



# Influence of $M_{23}C_6$ dissolution on the kinetics of ferrite to austenite transformation in Fe-11Cr-0.06C stainless steel

Alvise Miotti Bettanini<sup>a,\*</sup>, Lipeng Ding<sup>a,c</sup>, Jean-Denis Mithieux<sup>b</sup>, Coralie Parrens<sup>b</sup>, Hosni Idrissi<sup>a,c</sup>, Dominique Schryvers<sup>c</sup>, Laurent Delannay<sup>a</sup>, Thomas Pardoën<sup>a</sup>, Pascal J. Jacques<sup>a</sup>

<sup>a</sup>Institute of Mechanics, Materials and Civil Engineering, Université catholique de Louvain, Louvain-la-Neuve B-1348, Belgium

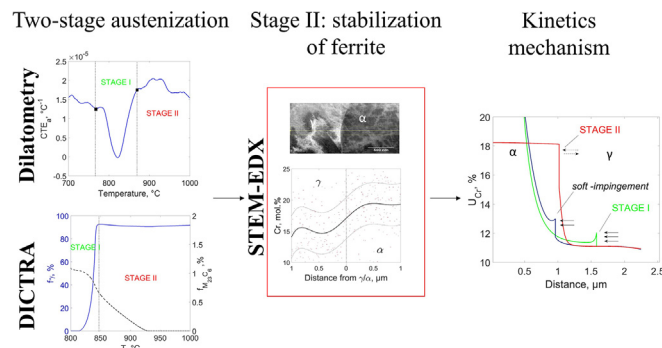
<sup>b</sup>Aperam Research Center, Isbergues BP 15, 62230, France

<sup>c</sup>Electron Microscopy for Materials Science (EMAT), Department of Physics, University of Antwerp, Antwerp 2020, Belgium

## HIGHLIGHTS

- The microstructure design of stronger martensitic stainless steels hinges on austenization kinetics.
- Cr-rich carbides controls the transformation kinetics due to Cr partitioning and stabilization of ferrite.
- Coarse carbides and fast heating rates lead to a soft-impingement of the Cr diffusion fields ahead of austenite interface.
- Ferrite-free microstructures can be produced for slow heating rate or smaller initial carbides.

## GRAPHICAL ABSTRACT



## ARTICLE INFO

### Article history:

Received 26 September 2018

Received in revised form 20 November 2018

Accepted 3 December 2018

Available online 6 December 2018

## ABSTRACT

The design of high-strength martensitic stainless steels requires an accurate control over the stability of undesired phases, like carbides and ferrite, which can hamper strength and ductility. Here, the ferrite to austenite transformation in Fe-11Cr-0.06C has been studied with a combined experimental-modelling approach. Experimental observations of the austenization process indicate that austenite growth proceeds in multiple steps, each one characterized by a different transformation rate. DICTRA based modelling reveals that the dissolution of the  $M_{23}C_6$  Cr-rich carbides leads to Cr partitioning between austenite and parent phases, which controls the rate of transformation through (i) a soft-impingement effect and (ii) consequent stabilization of the ferrite, which remains untransformed inside chromium-enriched-zones even after prolonged austenization stage. Slow heating rate and smaller initial particle sizes allow the design of ferrite-free microstructure.

© 2018 Published by Elsevier Ltd.

## 1. Introduction

The automotive industry is constantly striving for reduction of gas emission of vehicles. Together with the improvement of propelling technologies, the use of stronger and lighter materials as structural

components is necessary to comply with current safety and environmental regulations. Among the last generation of high strength steels, martensitic stainless steels (MSS) show an interesting combination of workability, strength and high temperature oxidation resistance, which are highly desirable for hot-stamping applications [1–4].

After rolling and annealing, Fe-Cr-C alloys present a structure close to thermodynamic equilibrium of ferrite and  $M_{23}C_6$  (M = Cr, Fe) carbides. In conventional industrial hot-stamping processes,

\* Corresponding author.

E-mail address: [alvise.miotti@uclouvain.be](mailto:alvise.miotti@uclouvain.be) (A. Miotti Bettanini).

**Table 1**  
Chemical composition of the as-received steel.

	C	Cr	Si	Mn	Ni	Nb	V	P	Cu	N	Fe
wt.%	0.06	11.0	0.4	0.5	0.4	0.10	0.083	0.02	0.04	0.025	Bal.
mol%	0.28	11.6	0.8	0.5	0.1	0.06	0.089	0.04	0.04	0.088	Bal.

the 1–2 mm thick steel sheets are rapidly heated to the austenitic temperature range to transform ferrite into austenite and to dissolve  $M_{23}C_6$  particles. Austenite is then transformed to martensite by rapid quenching to room temperature in the forming tools.

The strength of MSS increases with the volume fraction and carbon content of the martensitic phase as well as with the precipitation of hardening particles, such as MC (M = Nb,Ti) carbides [5–8]. On the other hand, the presence of residual ferrite leads to stress and strain heterogeneities during plastic deformation, which promotes ductile damage [9–17] and undermine the performance in terms of ductility and tensile strength [18–20]. Recent observations show that the mechanical strength contrast between ferrite and martensite increases the magnitude of the plastic strain and of the stress triaxiality in the former phase, thus accelerating the damage processes [21–24]. Hence, a deep understanding of the mechanisms controlling the kinetics of high-temperature ferrite to austenite transformation in order to design ferrite-free microstructure is of both fundamental and practical industrial interest.

Whereas the kinetics of austenization of Fe-C alloys is solely controlled by interstitial carbon diffusion [20,25], the presence of substitutional alloying elements can decrease the rate of austenite transformation by several orders of magnitude [26–36]. This effect is accentuated if the alloying elements are carbide formers like Cr and Nb, in which case a very strong interaction with carbon is expected [37,38].

For its predominantly technological relevance, the reversion of martensite to austenite in more complex, high alloy steels has been recently investigated using experimental and modelling methods [39–42]. In some cases, austenite growth is taking place over a broad temperature window and proceeds in multiple steps, each one characterized by a different transformation rate [43–45]. This is the case of 16Cr–4Ni SMSS (Super Martensitic Stainless Steel), which shows an initial fast austenization followed by a rapid decrease of the austenite growth rate at higher temperatures [44]. This was recently confirmed by in-situ synchrotron x-ray diffraction combined to thermodynamic simulations on a similar alloy [45]. By coupling the experimental observations with kinetics simulations in DICTRA [46], Nissen et al. have shown that the transition between the high and low growth rate could originate from the interaction of Cr and Ni profiles at the end of the transformation. This phenomenon, known as soft-impingement, describes the overlapping of diffusion fields ahead of the reaction front which is frequently observed in the late stage of austenite to ferrite transformation in steel [47–49].

A two-step austenization kinetics is often associated with carbides dissolution [50–56]. In Fe-Cr-C alloy, the dissolution of spherical  $M_{23}C_6$  and  $M_7C_3$  carbides and the simultaneous ferrite to austenite transformation were studied by Shtansky et al. [52] using high resolution transmission electron microscopy (HRTEM). In some cases, the dissolution of  $M_{23}C_6$  promotes the formation of a shell of ferrite, which remains untransformed during the austenization process. In another work, Beneteau et al. [54] observe a two-stage austenization in the presence of  $M_{23}C_6$  and  $Cr_2N$  particles in high nitrogen steel using in-situ X-ray diffraction. While a large amount of austenite (70 vol.%) forms rapidly between 845°C and 890°C, the end of the transformation is considerably slower, stretching from 890°C to 1025°C, and controlled by the rate of carbide dissolution. However, even though this strongly suggests a correlation between these events, a full understanding of the kinetics mechanisms could not be assessed from the results. Precipitation and dissolution of

intermetallics were again associated to a two-step austenization by Kapoor et al. [57] in precipitation hardening stainless steel, in which the austenization kinetics seemed to be controlled by element partitioning. On the other hand, Bojack et al. [43] found little evidence of the impact of the carbides dissolution on the ferrite to austenite transformation in high-Cr steel even though the latter shows a two-stage kinetics, typical of ferrite to austenite transformation in the presence of large compositional gradients. Thus, there is a need of additional studies to evaluate the extent of the interaction of the Cr-rich carbides dissolution and the austenite growth in high-Cr steel.

The goal of the present study is to scrutinise the complex interaction between carbides dissolution and ferrite to austenite transformation in a Fe-11Cr-0.06C alloy with an initial volume fraction of 1.1 vol.% of  $M_{23}C_6$  particles. The experimental results are compared to kinetics simulations performed using DICTRA, which is used to correlate the observed austenite growth rate to the underline kinetics mechanisms that control the transformation.

## 2. Experimental methods

A modified AISI 410 martensitic stainless steel was cast, hot rolled, annealed and pickled by Aperam Stainless Steel Europe. The chemical composition is reported in Table 1. The equilibrium microstructure at the annealing temperature predicted with Thermo-Calc consists of ferrite, 1.1 vol.% of  $M_{23}C_6$  (M=Fe,Cr) and 0.12 vol.% of NbC carbides. The A1, A3 and  $M_{23}C_6$  solvus temperatures calculated with the TCFe6 thermodynamic database of Thermo-Calc are 783°C, 826°C and 816°C, respectively.

The austenization heat treatments were carried out in a Bahr 805 A/D push rod dilatometer following the standard ASTM A1033-10(2015) [58]. Cylindrical samples 10 mm in length and 5 mm in diameter were machined from the aforementioned 6 mm thick sheets by electrical discharge machining (EDM) so that the rolling direction (RD) is aligned with the main axis of the cylinder. The desired heat-treatments were directly programmed. Temperature was monitored by means of a S-type thermocouple spot-welded at the centre of the surface of the cylindrical samples. They were heated to 1000°C at rates of 0.01°C/s, 0.5°C/s and 10°C/s, followed by isothermal holding at 1000°C for 1800 s(30 min). The samples were then quenched to room temperature using high pressure nitrogen ( $N_2$ ) ejected directly on the sample's surface. The initial cooling rate equals 80°C/s between 1000°C and  $M_s$ , then decreases sharply to 12°C between  $M_s$  and room temperature. This gives an overall cooling rate of 30°C/s. All heat treatments were performed under a pressure of  $1 \times 10^{-4}$  mbar to minimize oxidation at high temperature. The temperature at which austenite begins to form during heating ( $Ac_1$ ) and the temperature at which the ferrite to austenite transformation is complete during heating ( $Ac_3$ ) was determined on a separate sample as prescribed by the standard.

Samples for microstructure characterization were mechanically ground with SiC papers followed by polishing to 1  $\mu$ m diamond paste and 0.03  $\mu$ m OPS-A suspension for 30 min. The samples were then etched with Beraha reagent (0.28 g potassium disulphite,  $K_2S_2O_5$ , 20 ml HCl 37%, 100 ml distilled  $H_2O$ ) for 8 s at room temperature or alkaline  $KMnO_4$  at 60°C for 5 min. The latter reagent allowed the characterization of  $M_{23}C_6$  carbides with

scanning electron microscopy (SEM) equipped with a Bruker energy-dispersive X-ray spectroscopy (EDX) detector. Transmission electron microscopy (TEM) specimens were cut using a dual-beam focused ion beam (FIB)/SEM instrument (FEI Helios Nanolab 650). Scanning TEM energy dispersive X-ray (STEM-EDX) was performed in a FEI Osiris TEM operated at 200 kV and equipped with a CHEMIS-TEM detector. X-ray diffraction (XRD) with Cu  $K_{\alpha}$  radiation at 30 kV and 30 mA was performed to confirm the presence of  $M_{23}C_6$  carbides. Finally, quantitative image analysis was carried out using the open-source ImageJ software [59].

### 3. Results

#### 3.1. Dilatometry and metallographic observations

Fig. 1 (a) presents two SEM micrographs of the microstructure in the as-received conditions and before the austenization heat treatments, showing the presence of ferrite and of some carbides. While NbC particles with a mean size of 50 nm seem to be homogeneously distributed in the matrix,  $M_{23}C_6$  ( $M=Fe,Cr$ ), with a mean size of 500 nm, are preferentially clustered into bands along the rolling

direction. The mean ferrite grain size is equal to  $10 \mu\text{m} \pm 7 \mu\text{m}$  and the measured volume fraction of  $M_{23}C_6$  and NbC is equal to 1.16 vol.% and 0.12 vol.%, respectively. The XRD pattern of Fig. 1 (b) confirms the presence of face-centred-cubic (FCC) type  $M_{23}C_6$  particles in the body-centred-cubic (BCC) ferrite.  $M_{23}C_6$  diffraction peaks are displaced of about  $1 \theta$  to what has been already reported in literature [60]. This discrepancy could arise from the relative content of Fe and Cr in the crystal lattice, which would affect the lattice parameter of  $M_{23}C_6$ .

The  $Ac_1$  and  $Ac_3$  temperatures of the alloy, as determined with dilatometry measurements, correspond to  $780^\circ\text{C}$  and  $871^\circ\text{C}$ , respectively. Fig. 2 (a) shows the dilatometry results during the isochronal heating of the as-received sample for heating rates equal to  $0.01^\circ\text{C/s}$ ,  $0.5^\circ\text{C/s}$  and  $10^\circ\text{C/s}$ . Here, the strain  $\epsilon = \Delta L/L_0$  is plotted with respect to temperature. Any offset with respect to linear expansion corresponds to the growth of new phases or dissolution of carbides. A first large offset is detected around  $800^\circ\text{C}$ , which indicates the start of the transformation from BCC ferrite to the more closely packed FCC austenite. This transformation stretches from  $800^\circ\text{C}$  to just above  $900^\circ\text{C}$ , the start and finish temperatures depending on the heating rate. Table 2 summarises the austenite start temperature ( $A_s^1$ ) and the

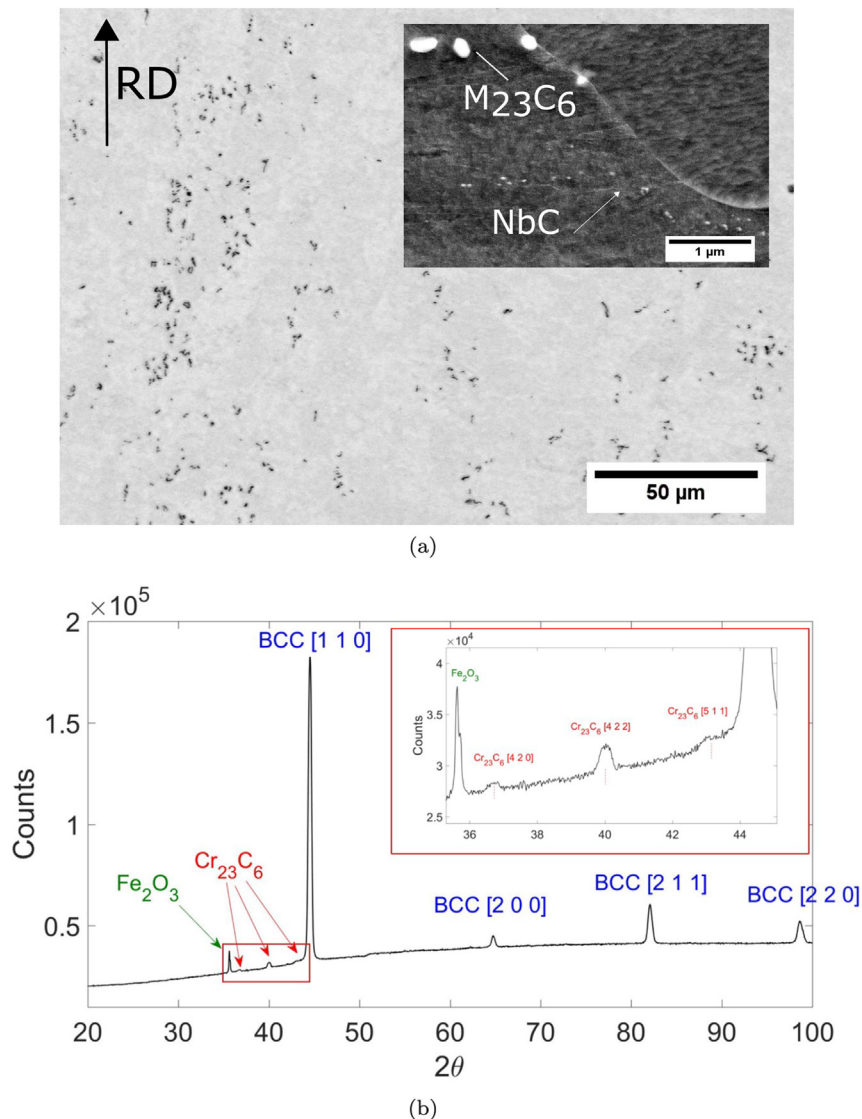
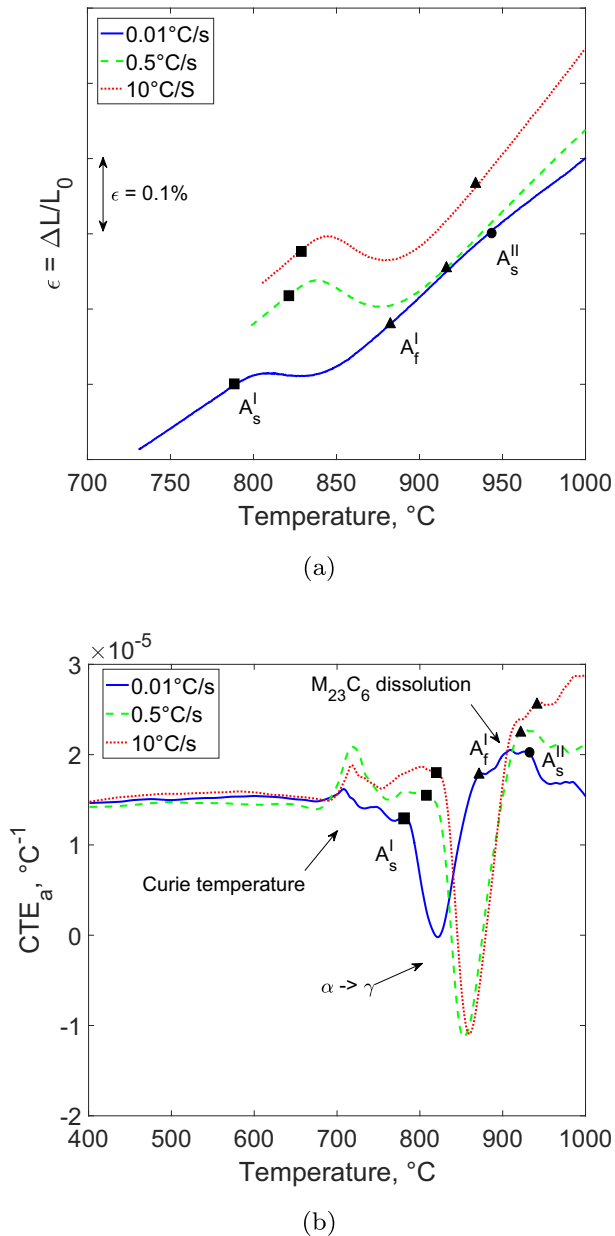


Fig. 1. (a) SEM micrographs showing  $M_{23}C_6$  carbides distributed inside the ferrite matrix along bands in rolling direction and a higher magnification view of  $M_{23}C_6$  and NbC carbides. (b) X-ray diffraction pattern of BCC-ferrite and enlarged peaks that confirm the crystallographic structure of FCC- $M_{23}C_6$  carbides.



**Fig. 2.** (a) Variation with temperature of the relative change of length (strain) and (b) the apparent coefficient of thermal expansion ( $CTE_a$ ) during isochronal heating at 0.01°C/s, 0.5°C/s and 10°C/s. The start ( $A_s^I$ ) and finish ( $A_f^I$ ), of the first stage of ferrite to austenite transformation, the subsequent  $M_{23}C_6$  dissolution and the beginning of the last stage of ferrite to austenite transformation,  $A_s^{II}$ , can be clearly identified in (b).

temperature at the end of the first austenite growth stage ( $A_f^I$ ) for the different heating rates. Both  $A_s^I$  and  $A_f^I$  temperatures increase with heating rate.

The derivative of the relative change of length  $d(\Delta L/L_0)/dT$ , referred to as the apparent coefficient of thermal expansion ( $CTE_a$ ), is shown in Fig. 2 (b). It reveals small deviations from linearity that were not clearly observed in Fig. 2 (a). Below the magnetic transformation (Curie temperature,  $T_c = 700^\circ\text{C}$ ),  $CTE_a$  is equal to  $15 \times 10^{-6} \text{ }^\circ\text{C}^{-1}$ . Moreover, between  $400^\circ\text{C}$  and  $T_c$ , the measured  $CTE_a$  remains constant, which indicates that no significant microstructural transformation related to changes in samples dilatation takes place in this temperature range. Above  $T_c$ , a large  $CTE_a$  reduction indicates the start of the ferrite to austenite transformation. Next,  $CTE_a$  increases again to values above  $20 \times 10^{-6} \text{ }^\circ\text{C}^{-1}$  before decreasing, although

**Table 2**

Experimentally determined temperatures for the onset of first ( $A_s^I$ ), second ( $A_f^I$ ) and last austenization stage ( $A_s^{II}$ ) for the three heating rates.

Heating rate	$A_s^I$ (°C)	$A_f^I$ (°C)	$A_s^{II}$ (°C)
0.01°C/s	783	874	945
0.5°C/s	810	922	> 1000
10°C/s	820	938	> 1000

only in the case of samples heated at 0.01°C/s, to values just above  $15 \times 10^{-6} \text{ }^\circ\text{C}^{-1}$ .

In order to better identify which phase transformation causes the observed  $CTE_a$  variations, samples corresponding to each heating rate were quenched from  $T=A_f^I$  and  $T=1000^\circ\text{C}$  to freeze the high temperature microstructures. Fig. 3 (a,b) shows the amount of residual ferrite and of undissolved  $M_{23}C_6$  carbides at these temperatures during isochronal heating at 0.01°C/s, 0.5°C/s and 10°C/s. About 22 vol.% of residual ferrite is still untransformed at  $T=A_f^I$  for the lowest heating rate, while, in the case of the heating rate at 0.5°C/s and 10°C/s, the amount of ferrite is equal to 6 vol.% and 3 vol.%, respectively. The same trend is observed for undissolved  $M_{23}C_6$  particles. Even though about 0.5 vol.% of  $M_{23}C_6$  carbides is still undissolved at  $T=A_f^I$  in the case of 0.01°C/s, only 0.1 vol.% of  $M_{23}C_6$  is present at higher heating rates. At  $T=1000^\circ\text{C}$ , the residual ferrite completely transforms to austenite for samples heated at 0.01°C/s. On the other hand, almost no austenite growth is observed at  $1000^\circ\text{C}$  for 0.5°C/s and 10°C/s.

In order to investigate the presence of the residual ferrite well above the calculated  $A_3$  temperature for the composition presented in Table 1, the local concentration of elements was probed with SEM-EDX and STEM-EDX. Fig. 4 (a) shows the microstructure at  $1000^\circ\text{C}$  for samples heated at 10°C/s. Darker islands of ferrite, which are preferentially oriented in the rolling direction, are embedded in the martensite matrix (transformed austenite). The concentration of elemental Cr measured by SEM-EDX is presented in Fig. 4 (b), which reveals an enrichment of Cr in the islands of residual ferrite. The local concentration of Cr in the ferrite ranges from 20 mol % to 25 mol %, which is significantly higher than the nominal steel composition. In addition, samples for STEM-EDX were machined by FIB to quantitatively characterize the Cr concentration gradient at the interface between residual ferrite and martensite. Fig. 4 (c) shows the bright field TEM micrograph of the interface machined by FIB in the location indicated in Fig. 4 (a), while Fig. 4 (d) displays the respective concentration of Cr across this boundary. The solid blue line in Fig. 4 (d) represents the average value of Cr concentration between the respective standard deviation (dotted lines). This additional characterization confirms the presence of a steep Cr gradient at the interface between martensite (approximately 15 mol % Cr) and ferrite (approximately 20 mol % Cr).

Finally, the specimens were held at  $1000^\circ\text{C}$  for 30 min to complete the austenite transformation. Fig. 5 shows a significant contraction for samples previously heated at 0.5°C/s and 10°C/s. This indicates transformation of residual ferrite into the more closely packed lattice of austenite phase. On the other hand, in agreement with the microstructural observations shown in Fig. 3, no significant transformation is detected for samples previously heated at 0.01°C/s, which confirms that austenitization is complete before the isothermal holding. Also shown in Fig. 5, is an unusual large dilatation for the sample previously heated at 10°C/s. This dilatation lasts for about 80 s of the isothermal holding, followed by a contraction and it is due to the dissolution of  $M_{23}C_6$  particles still present in the microstructure at  $1000^\circ\text{C}$ .

### 3.2. DICTRA modelling

In order to highlight the thermodynamics and kinetics mechanisms driving the observed three-stage austenization, a simulation

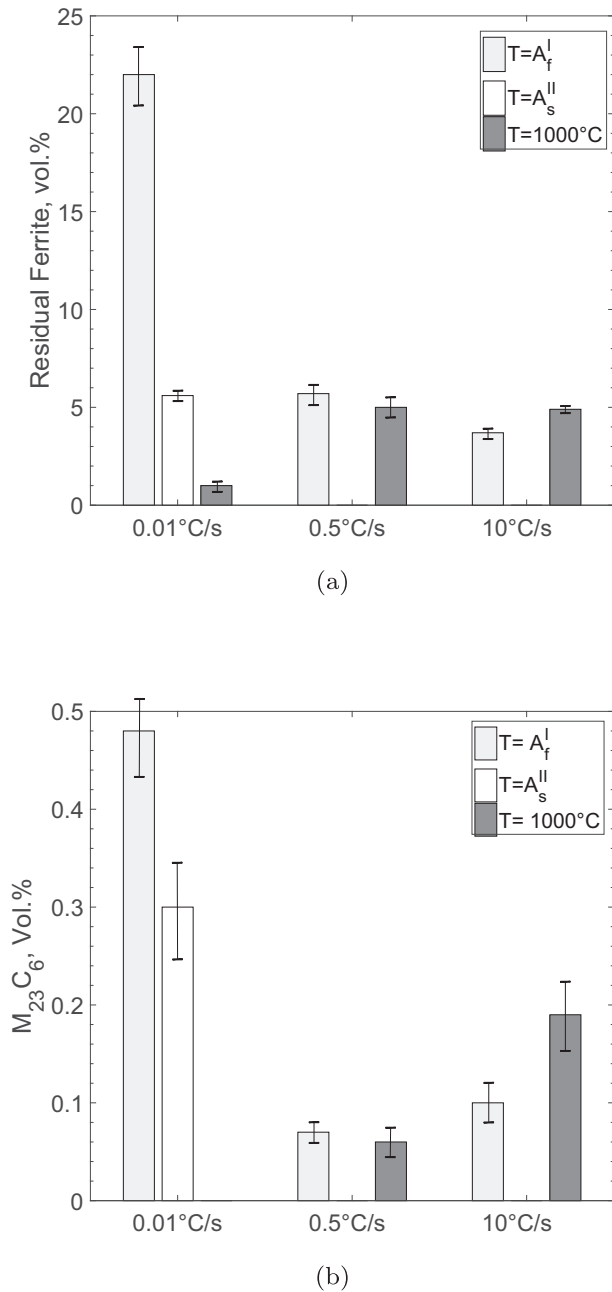


**Fig. 3.** Amounts of (a) residual ferrite and (b)  $M_{23}C_6$  carbides after interruption of the heat treatment followed by rapid quenching at  $T=A_f^I$ ,  $T=A_f^{II}$ , and  $T=1000^\circ\text{C}$  for isochronal heating at 0.01°C/s, 0.5°C/s and 10°C/s, respectively.

of the austenite growth and simultaneous dissolution of  $M_{23}C_6$  particles in ferrite was carried out with the help of the software DICTRA [46,61]. The considered system is illustrated in Fig. 6, which conforms to the metallographic observations prior to the heat treatment and consists of a spherical  $M_{23}C_6$  particle embedded in a ferrite matrix. Austenite is expected to nucleate in the surrounding and to grow inwards in the direction of the carbide particle. The initial composition of the carbide and the surrounding matrix is determined with an equilibrium calculation at  $725^\circ\text{C}$  with the software Thermo-Calc and it is given in Table 3. The size of the  $M_{23}C_6$  carbide is set to 500 nm and the total size of the cell ensures that its volume fraction is equal to the experimental value of 1.1 vol.%. The solvus temperature of NbC, for the composition listed in Table 1,

is equal to  $1142^\circ\text{C}$ , therefore NbC particles are not expected to significantly affect the austenization kinetics at  $1000^\circ\text{C}$ . On the other hand, the presence of 0.12 vol.% of NbC changes the concentration of carbon and other alloying elements in ferrite and  $M_{23}C_6$  carbide. This effect is included in the initial conditions of the DICTRA simulations. Thermodynamics and kinetics data were taken from the TCFE6 and MOB2 databases while the ferrite to austenite transformation was modelled with the moving boundary model of DICTRA v.26, that enforces local thermodynamic equilibrium at the interfaces between the three phases ( $M_{23}C_6$ , ferrite and austenite). Only four elements are considered: Fe, C, Cr and Ni.

Fig. 7 (a,c) presents the results of the kinetics modelling for heating rates equal to 0.01°C/s, 0.5°C/s and 10°C/s, respectively, with the volume fraction of austenite and  $M_{23}C_6$  particles plotted against temperature. The simulations successfully reproduce the fast and slow growth regimes observed experimentally. Austenite nucleation is predicted at  $810^\circ\text{C}$ ,  $815^\circ\text{C}$  and  $822^\circ\text{C}$  for the heating rate of 0.01°C/s, 0.5°C/s and 10°C/s, respectively. Austenite then rapidly grows in ferrite up to volume fractions between 70 vol.% and 95 vol.% for the lowest and highest heating rates, respectively. Finally, the growth rate rapidly decreases, corresponding to the beginning of the second stage of austenization, during which  $M_{23}C_6$  particles rapidly dissolve into the nearby ferrite. At  $T=850^\circ\text{C}$ , the residual volume fraction of  $M_{23}C_6$  is 0.1 vol.%, 0.6 vol.% and 1 vol.% for the heating rate equal to 0.01°C/s, 0.5°C/s and 10°C/s, respectively. During the second stage, DICTRA predicts zero austenite growth or, in the case of 10°C/s, even a decrease of the austenite volume fraction as a consequence of ferrite growth.  $M_{23}C_6$  dissolution ends at  $A_f^{II}$ , which marks the onset of the last austenization stage characterized by a slow growth of austenite into the residual ferrite. From these results, the interaction between  $M_{23}C_6$  dissolution and the shift between stage I and stage II of the growth rate seems apparent. Finally, fully austenitic microstructure is predicted after prolonged holding at  $1000^\circ\text{C}$ , as shown by the evolution of the austenite volume fraction with time for a heating rate of 0.5°C/s and 10°C/s in Fig. 8 (a,b). The ferrite to austenite transformation is completed after 2000 s (about 33 min) and 1 h of isothermal holding at  $1000^\circ\text{C}$  for heating rates of 0.5°C/s and 10°C/s, respectively.

According to Fig. 7 (a,c), the transition of kinetics, as observed experimentally, seems to be strongly related to the dissolution of the  $M_{23}C_6$  particle. Hence, additional simulations were carried out to investigate the possible effect of initial carbide size on the transformation rate, while the initial volume fraction is kept constant and equal to  $V_0 = 1.1$  vol.%. Fig. 9 shows the evolution of the austenite volume fraction during heating at 0.5°C/s for initial  $M_{23}C_6$  size,  $d_0$ , of 100 nm or 1000 nm. A smaller initial carbide size promotes faster austenite transformation and smoother transition between the two growth regimes. When  $d_0 = 100$  nm, the  $M_{23}C_6$  carbides are completely dissolved at  $926^\circ\text{C}$ , whereas dissolution is delayed to  $986^\circ\text{C}$  when  $d_0 = 1000$  nm. At  $1000^\circ\text{C}$ , these different dissolution rates respectively produce a fully austenitic structure and a dual phase microstructure with 15 vol.% of residual ferrite.

## 4. Discussion

### 4.1. Dilatometry experiments and DICTRA simulations

The dilatometric measurements of ferrite to austenite transformation presented in Fig. 2 (a,b) and the ex-situ metallographic observations in Fig. 3 (a,b) reveal a complex mechanism of ferrite transformation, which seems to take place in multiple steps, as previously reported in the literature for alloys of similar composition [43,44]. Even if the accuracy of dilatometry measurements of phase transformations was recently questioned on the basis of comparable densities of martensite and austenite at high temperature

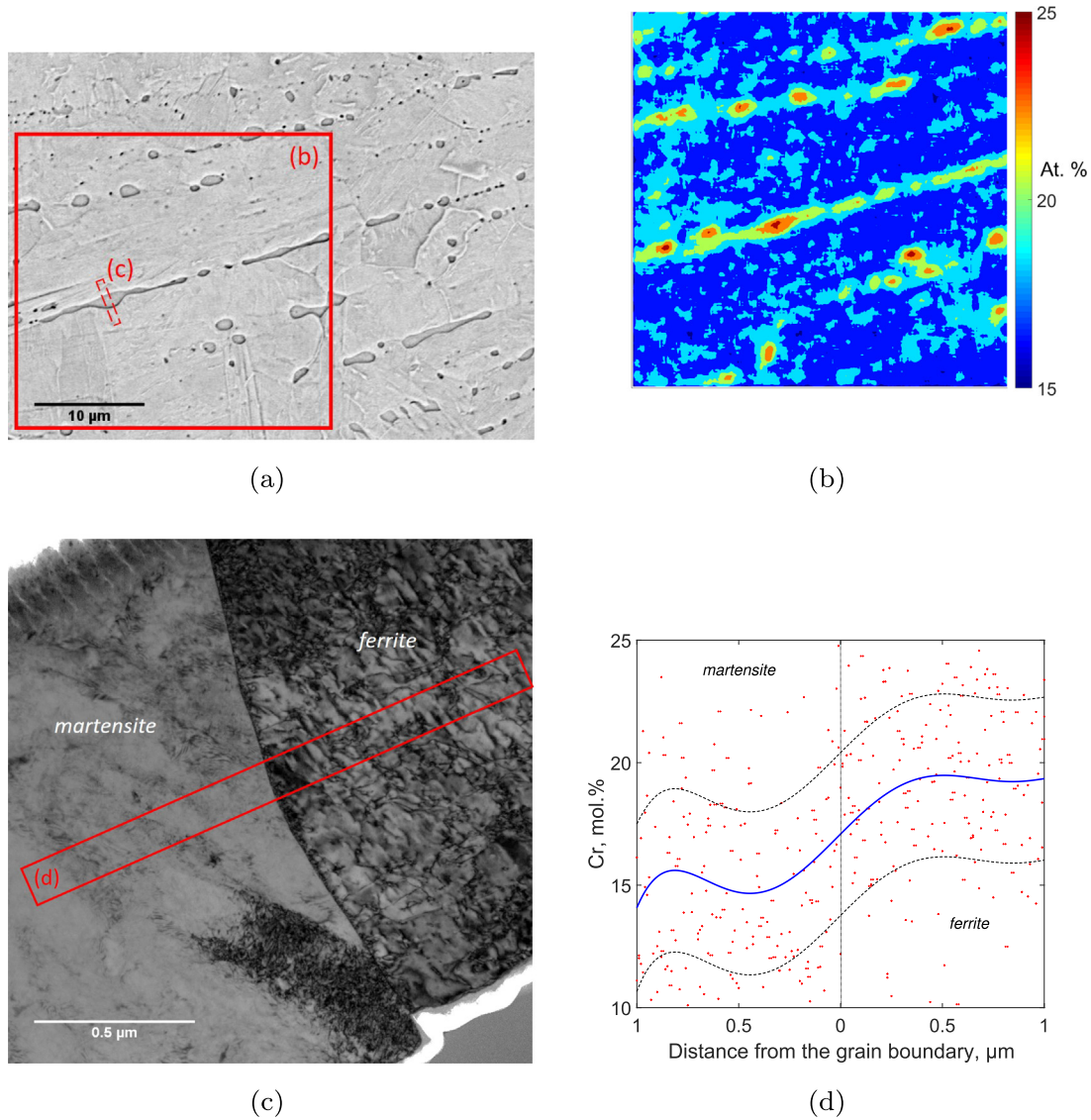


**Fig. 4.** (a) SEM micrograph of the room temperature microstructure quenched from 1000°C for a sample previously heated at 10°C/s. (b) SEM-EDX mapping of Cr mole fraction over an area indicated in (a). (c) Bright field TEM and (d) STEM-EDX analysis of Cr mole fraction across the interface between martensite (transformed austenite) and residual ferrite. The blue line in (d) represents the average value of the measurements and the standard deviation (dotted lines).

(above 850°C) [62,63], when carefully analysed,  $CTE_a$  is representative of the ferrite to austenite transformation [64]. The measured  $CTE_a$  values between 400°C and the Curie temperature confirm that no other precipitation occurs on heating and its mean value is consistent with  $CTE_a$  of ferrite for similar alloy composition [56]. At  $T = A_s^I$ , the first  $CTE_a$  reduction shown in Fig. 2 (b) corresponds to the main ferrite to austenite transformation. Next,  $T = A_f^I$  marks the end of the first stage of rapid ferrite to austenite transformation and the onset of dissolution of  $M_{23}C_6$  carbides. Due to the larger lattice atomic volume [65] of  $M_{23}C_6$  carbides compared to the one of ferrite or austenite, a dissolution of such carbides should lead to a net contraction. However, the dissolution of  $M_{23}C_6$  particles releases Cr and C atoms in the matrix, which increases the lattice constant of ferrite and austenite, respectively [56,66]. This leads to a net dilatation of the samples, as shown in Fig. 2 (b). Moreover, at least in the case of the lowest heating rate of 0.01°C/s, metallographic observations summarised in Fig. 3 (b) confirm that the  $CTE_a$  increases due to the dissolution of  $M_{23}C_6$  particles, which are

completely dissolved at 1000°C. In addition, the maximum  $CTE_a$  values during  $M_{23}C_6$  dissolution change depending on the heating rate, which confirms that the dissolution rate strongly depends on the processing conditions, as previously reported [50]. Indeed, Fig. 2 (b) suggests that for a heating rate of 0.5°C/s and 10°C/s the complete dissolution of  $M_{23}C_6$  particles is delayed to the isothermal holding at 1000°C. Finally, the  $CTE_a$  reduction at 918°C for the heating rate of 0.01°C/s corresponds to the completion of ferrite to austenite transformation, as confirmed by the metallographic observations in Fig. 3 (a).

As discussed above, phase transformation seems to be highly dependent on the chosen heating rate. In the case of the slow heating rate (0.01°C/s), austenite shows a two-stage growth regime, the first one between 800°C and 850°C, while the second one starts above 925°C. On the other hand, austenite fraction increases up to around 95 vol.% in one single step during isochronal heating at 0.5°C/s and 10°C/s. Furthermore, austenite does not grow up to isothermal holding at 1000°C, during which

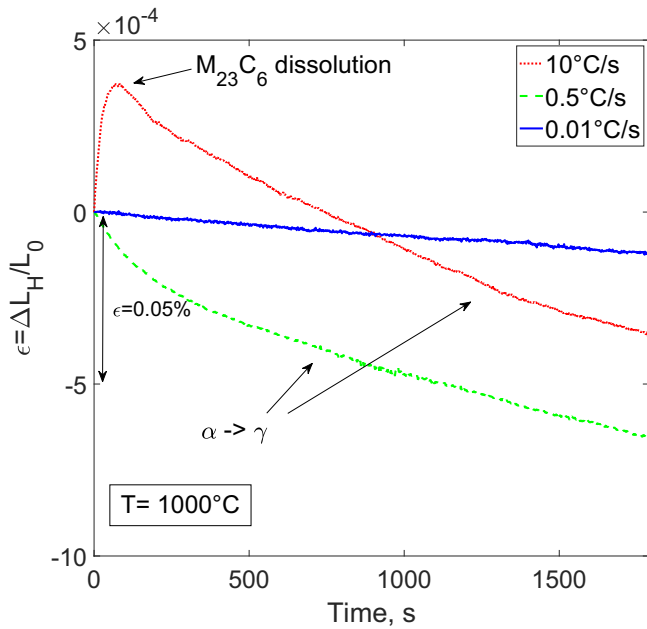


**Fig. 5.** Relative change of length,  $\Delta L_H/L_0 = (\Delta L - \Delta L_{H0})/L_0$ , for the isothermal heat treatment at 1000°C for the three samples previously heated at 0.01°C/s, 0.5°C/s and 10°C/s, respectively.

residual ferrite eventually transforms to austenite. In other words, for faster heating rates, the second stage of austenite transformation is delayed to the isothermal holding at 1000°C. These conclusions agree with recent results reported by Bojack et al. [43].

DICTRA simulations are in fairly good agreement with the experimental measurements of austenite transformation kinetics. While

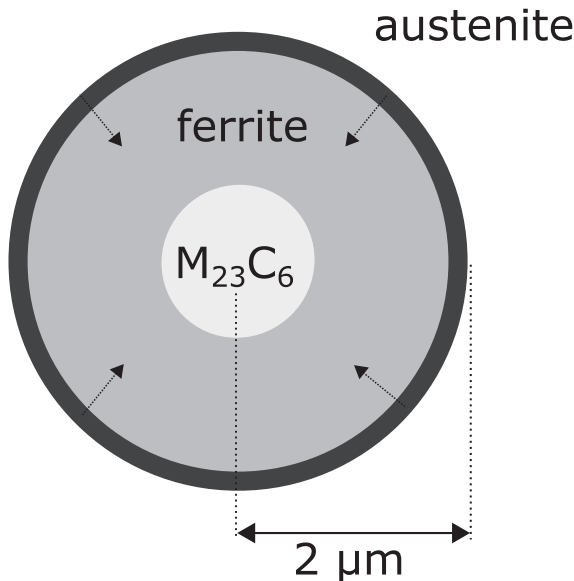


**Fig. 6.** Schematic representation of the system considered for the modelling with DICTRA. The initial configuration represents the microstructure after the batch annealing and prior to the austenization heat treatment. A spherical  $M_{23}C_6$  particle ( $R = 500$  nm, vol. fraction = 1.1%) is embedded within the ferrite matrix. Austenite is initially set as an inactive phase, which is allowed to nucleate at the cell boundaries when the system meets the thermodynamic conditions for austenite nucleation.

**Table 3**

Composition of  $M_{23}C_6$  and ferritic matrix at the beginning of the DICTRA simulation determined by an equilibrium calculation at 725°C in ThermoCalc with TCFe6 database.

Elements	Ferrite (wt.%)	$M_{23}C_6$ (wt.%)
Cr	10.69	71.28
C	0.00058	5.59
Ni	0.4	0.051
Fe	bal.	bal.

austenite nucleation temperature ( $A_s^I$ ) is well-captured by the simulations, the  $A_f^I$  temperature is underestimated by about 43°C, 77°C and 82°C for 0.01°C/s, 0.5°C/s and 10°C/s, respectively. This discrepancy can be rationalized based on different factors. First of all, only four major elements, namely Fe, Cr, Ni and C, are included in the DICTRA model. However, other elements like Mn and Si, which are not considered, are known to strongly affect the kinetics of austenite growth in steel [29]. Furthermore, only an average  $M_{23}C_6$  volume fraction is considered. While this choice greatly simplifies the simulation, the true local  $M_{23}C_6$  volume fraction is likely to have important consequences on austenite nucleation and growth. It was indeed observed that  $M_{23}C_6$  particles are elongated and segregated in bands along the principal rolling direction, which is a consequence of the segregation of Cr and other alloying elements during the casting process [67]. Hence, austenite is likely to nucleate at lower temperatures and to quickly grow outside these Cr-rich bands, while the opposite is true in regions of higher local volume fraction of  $M_{23}C_6$  particles. Thus, while DICTRA simulations describe the average behaviour of the real system, the austenite start ( $A_s^I$ ) and austenite finish ( $A_f^I$ ) temperatures are, in practice, scattered in a broad temperature window.

Finally, the size distribution and morphology of carbide particles in the real material are other important factors that might control the transformation kinetics. On the one hand, Fig. 9 clearly shows the effect of carbide size on its dissolution kinetics and, as a consequence, on the ferrite to austenite transformation. Smaller carbides dissolve faster, thus increasing the rate of ferrite transformation. Hence, in order to better represent the true particle distribution seen experimentally, a multi-cell simulation, although more computationally demanding, would better reproduce the experimental observations at the beginning of the transformation process [68]. On the other hand, the initial morphology of  $M_{23}C_6$  particles has been found to not significantly influence the kinetics of the transformation. An additional DICTRA simulation for an initial cylindrical configuration, in which the  $M_{23}C_6$  particle is considered as an elongated cylinder (aspect ratio,  $AR \gg 1$ ) results in a  $M_{23}C_6$  dissolution and growth of austenite comparable to the case of spherical particle ( $AR=1$ ). The  $M_{23}C_6$  particle dissolution temperature equals 929°C and 941°C for a spherical and cylindrical configuration, respectively. Hence, the actual morphology of carbides is not expected to significantly impact the overall transformation kinetics.

#### 4.2. Description of the kinetics mechanisms

As already suggested in past researches on austenite formation in high alloy steels, but never directly observed in the case of MSS, the inhomogeneous distribution of alloying elements across the microstructure strongly influences the austenization process. Fig. 10 (a,c) shows the concentration gradient of Cr in the simulation cell at different temperatures for the three considered heating rates in this study. The amount of Cr is given as the site fraction occupied by Cr atoms in the lattice,  $U_{Cr}$ , defined as  $U_{Cr} = X_{Cr}/(1 - X_C)$ , where  $X_{Cr}$  and  $X_C$  are the mole fractions of Cr and C atoms, respectively. With

reference to Fig. 10, austenite nucleates from the periphery (right-hand side of the figure) and grows towards the centre (left-hand side of the figure), where it meets an increasing Cr gradient due to the dissolution of the  $M_{23}C_6$  particle. Based on the analysis of the  $U_{Cr}$  profiles, the three austenization stages outlined in Fig. 7 can be rationalized as follows:

- Stage I: nucleation and rapid growth of austenite  
 Cr profiles at  $T=820^\circ\text{C}$  for  $0.01^\circ\text{C/s}$ ,  $0.5^\circ\text{C/s}$  and  $T=840^\circ\text{C}$  for  $10^\circ\text{C/s}$  reveal the Cr gradient present in the cell immediately after the nucleation of austenite (at the periphery of the simulation cell). During the first rapid growth, two gradients of Cr develop: the first one originates from the partial dissolution of  $M_{23}C_6$  (on the left-hand side of the cell) while the second one follows the fast displacement of the ferrite/austenite interface, which, for higher heating rates, produces a “spike” of Cr concentration in front of the interface as shown in Fig. 10 (b,c). Hence, below  $T=A_s^I$ , the rapid growth of austenite seems to be sustained by diffusion of Cr in the ferrite, which is thus enriched in Cr.

- Stage II: soft-impingement and austenite growth stasis  
 At  $T=A_s^I$ , which is equal to  $830^\circ\text{C}$ ,  $845^\circ\text{C}$  and  $855^\circ\text{C}$  for  $0.01^\circ\text{C/s}$ ,  $0.5^\circ\text{C/s}$  and  $10^\circ\text{C/s}$ , respectively, the two aforementioned Cr gradients overlap. This marks the beginning of the so-called soft-impingement effect, which drastically changes the driving force for Cr diffusion inside the simulation cell and produces the kinetics shift shown in Fig. 7 (a,c). As a result, the transformation front slows down and eventually stops.
- Stage III: slow austenite growth  
 As the temperature is increased above  $T=A_s^I$ , the Cr profiles in Fig. 10 (a,b) indicate a homogenization of Cr in ferrite at  $T=865^\circ\text{C}$  and  $T=935^\circ\text{C}$  for  $0.01^\circ\text{C/s}$  and  $0.5^\circ\text{C/s}$ , respectively. This temperature, named  $A_s^{II}$ , marks the complete dissolution of  $M_{23}C_6$  particles and the onset of the last austenization stage. The Cr gradient that results from soft impingement does not allow any net atom diffusion from the interface towards the ferrite. At this point, the interface displacement is solely controlled by the diffusion of Cr atoms inside the austenite, which results in a net reduction of the austenization rate. On the other hand, Fig. 10 (c) shows that, in the case of a high heating rate of  $10^\circ\text{C/s}$ , Cr is not yet homogenized in ferrite at  $1000^\circ\text{C}$ . This event delays ever further the start of the last austenization stage.

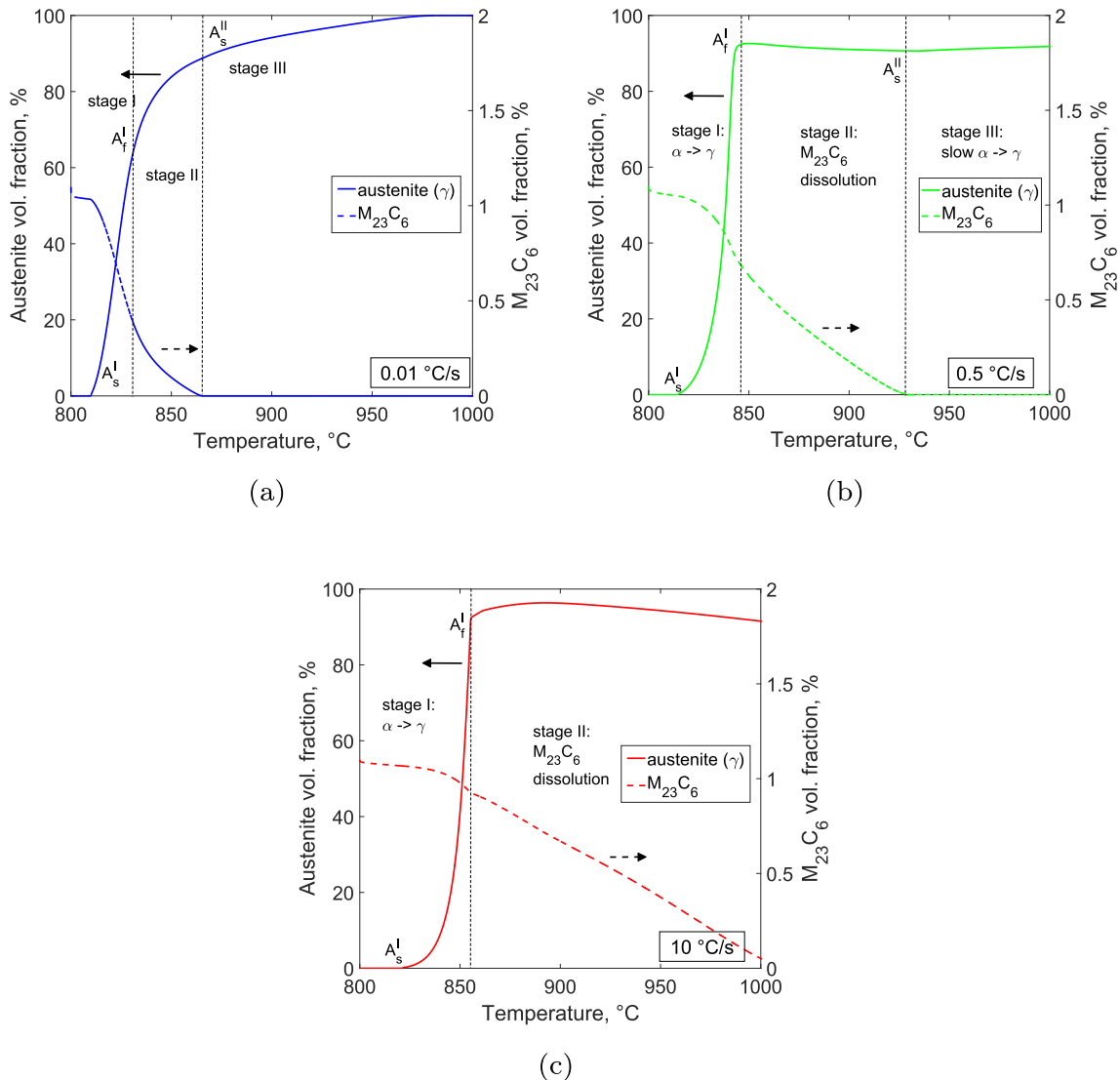
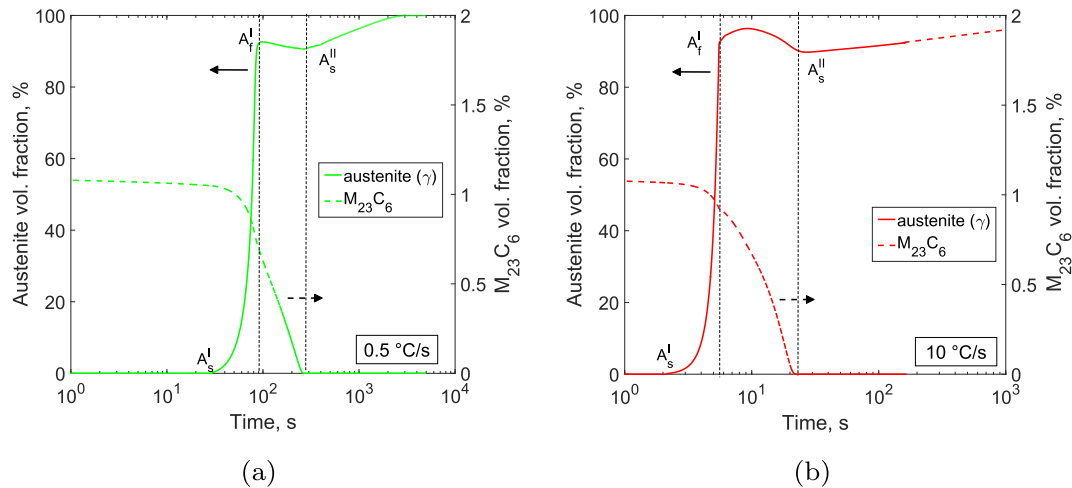


Fig. 7. DICTRA predictions of the austenite growth (left-hand axis) and of the  $M_{23}C_6$  dissolution (right-hand axis) during the isochronal heating stage for heating rates equal to (a)  $0.01^\circ\text{C/s}$ , (b)  $0.5^\circ\text{C/s}$  and (c)  $10^\circ\text{C/s}$ , respectively.





**Fig. 8.** DICTRA prediction of austenite growth (left-hand axis) and of  $M_{23}C_6$  dissolution (right-hand axis) as a function of time for heating rates equal to (a) 0.5 °C/s and (b) 10 °C/s, respectively.

#### 4.3. Effect of microstructure and process conditions

The  $M_{23}C_6$  dissolution has been found to significantly affect the kinetics of ferrite to austenite transformation, hence the resulting microstructure at 1000 °C. This effect is confirmed by the results of the DICTRA simulations in Fig. 9, which show the effect of the initial size of the  $M_{23}C_6$  particles on the transformation process. Smaller  $M_{23}C_6$  particles dissolve faster and at lower temperature than larger initial particles. As a result, the extent of Cr enrichment and soft-impingement is smaller in the former case, while a stronger interaction between  $M_{23}C_6$  dissolution and austenite growth is predicted for larger  $M_{23}C_6$  particles. In this sense, the initial size of the  $M_{23}C_6$  carbides is a critical microstructure parameter that, together with the heating rate, controls the austenization kinetics [50,69]. This result confirms recent simulations of austenization in low alloy steels in the presence of cementite [70].

Even in the case of martensite to austenite transformation in high-Cr steels, the presence of a low fraction (1–2 vol.%) of  $M_{23}C_6$  or  $M_6C$  carbides could significantly influence the austenization process. In a recent work, Bojack et al. found that two-stage austenization

in 13Cr6Ni2Mo SMSS is promoted by the simultaneous dissolution of Cr-rich and Mo-rich carbides, which delays austenite growth and enhances the two-stage character of the transformation [43]. Even though they do not provide any quantitative evidences, they suggested that the distribution of alloying elements during the transformation could be the origin of this phenomenon, as observed in Fig. 10 (a,c).

In addition, the austenization depends on the processing parameters, as established with the experimental results and DICTRA simulations. It was found that the heating rate has a strong effect on the austenization kinetics. In general, larger heating rates increase the austenite nucleation temperature,  $A_f^I$ , and the final temperature of the first stage of austenization,  $A_f^I$ . This is a well-known phenomenon that originates from, and confirms, the diffusional mechanism of austenite growth for conventional heating rates [71,72]. Furthermore, for a heating rate of 10 °C/s, the onset of the third stage is delayed until the isothermal holding, which results in a large contraction of the sample as a consequence of continuous austenite formation. The same effect is reported for multi-stage transformation kinetics in SMSS [43,44].

DICTRA simulations confirmed that the soft-impingement effect in the ferrite increases with the heating rates. Higher heating rates accelerate the initial transformation rate, thus increasing the Cr composition pile-up in front of the ferrite/austenite interface. As the dissolution rate of  $M_{23}C_6$  particle increases, the flux of Cr atoms in ferrite increases. This produces a larger Cr gradient in the ferrite with a subsequent increase of the soft-impingement effect. Since the onset of the second stage requires prior homogenization of Cr inside the ferrite, a high heating rate delays the transformation of residual ferrite to austenite. A similar effect of heating rate on transformation kinetics was recently observed in SMSS by Niessen et al. [45] using DICTRA simulations.

On the other hand, slow heating rates, which produce fully austenitic microstructures at 1000 °C, are not industrially viable due to the very long processing time. Thus, although the primary goal of this work is to shed light on the fundamental kinetics mechanisms controlling the phase transformation, further work is needed to design optimised thermal profiles subject to the concurrent objectives of minimizing time while maximizing austenite fraction.

#### 4.4. Thermodynamic considerations on the stability of ferrite

An additional effect of the high heating rate is the transient stabilization of ferrite as a consequence of Cr enrichment, which remains

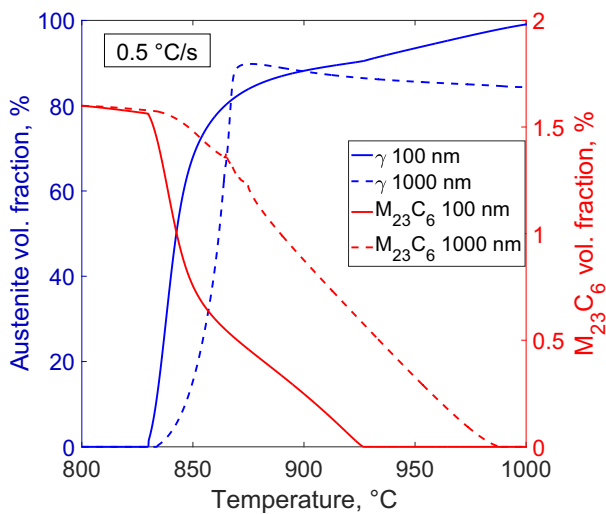


**Fig. 9.** Predictions of DICTRA kinetics model of the evolution of austenite and  $M_{23}C_6$  volume fraction at a heating rate equal to 0.5 °C/s for two initial carbide sizes ( $d_0$ ) equal to 100 nm and 1000 nm, respectively.

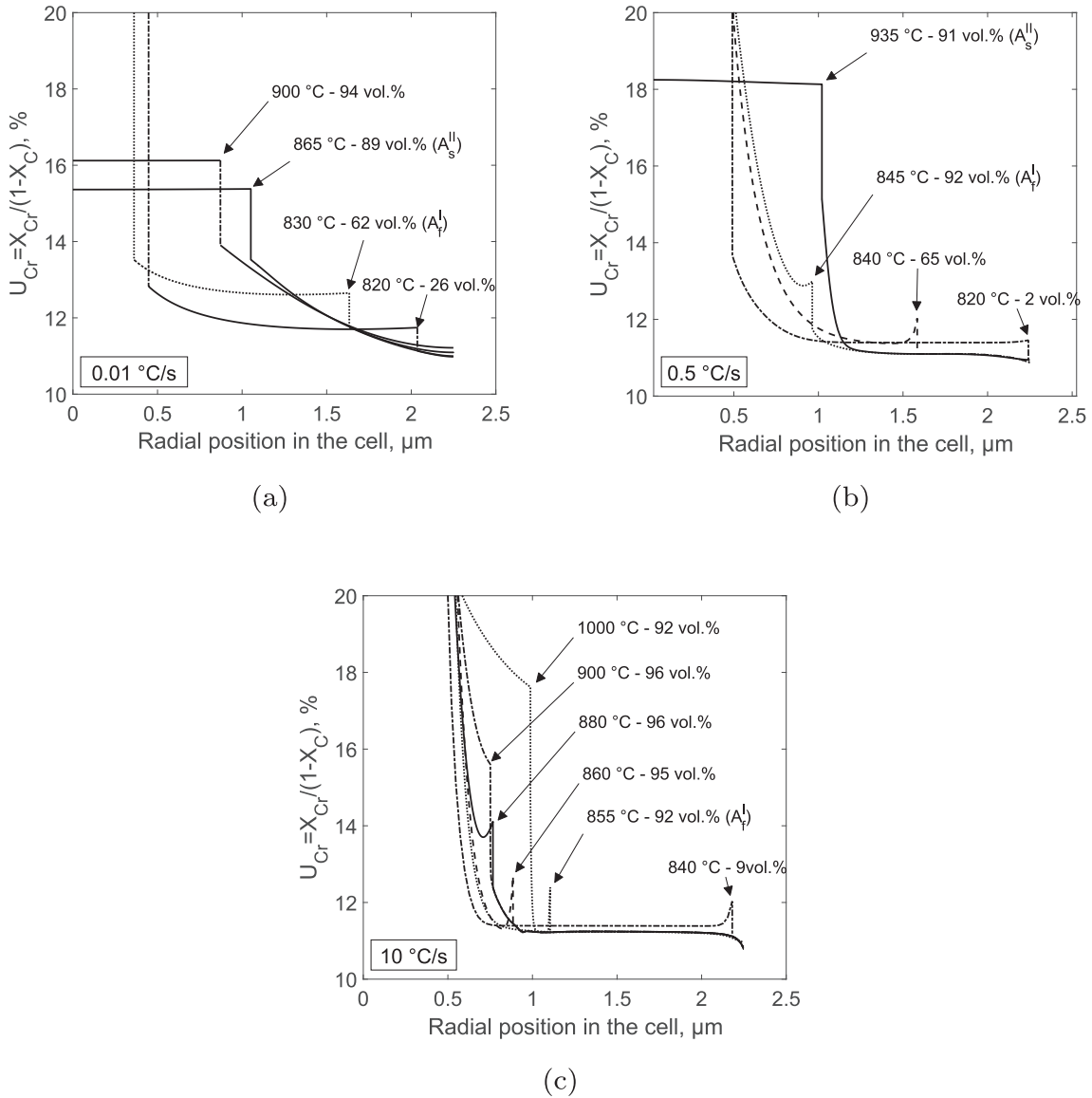


**Fig. 10.** Cr content (site fraction) vs. distance from the centre of the DICTRA simulation cell (Fig. 6) at different temperatures during isochronal heating at a heating rate equal to a) 0.01 °C/s, b) 0.5 °C/s and c) 10 °C/s. Austenite grows from the periphery (right-hand side of the graphs), while  $M_{23}C_6$  dissolves in the centre (left-hand side of the graphs). The ferrite/austenite interface is indicated by the arrows in each figure, which also reports the volume fraction of austenite.

untransformed even above the A3 temperature for the nominal steel composition in Table 1. This stabilization is evident from the DICTRA simulations in Fig. 8 (b), which even predicts an increment of the fraction of residual ferrite between  $A_f^I$  and  $A_f^{II}$  for the heating rate of 10 °C/s. This is readily explained based on thermodynamic considerations. Fig. 11 (a) shows the isothermal phase diagram of the ternary Fe-Cr-C system at 900 °C and the average composition of the residual ferrite from DICTRA calculations at the same temperature (■), which corresponds to the beginning of the ferrite growth. At this point, the composition of the residual ferrite falls well within the thermodynamic stability domain of the BCC ferrite in the phase diagram. However, as the temperature is further increased, the system will eventually meet the thermodynamic condition for austenite growth, as shown in Fig. 11 (b). After 10 s of holding at 1000 °C, the average composition of the residual ferrite (★) quickly falls into the two-phase ferrite-austenite region, meeting the condition for austenite growth.

The presence of Chromium Enriched Zone (CEZ) after austenization at 10 °C/s was previously observed with SEM-EDX and STEM-EDX in Fig. 4 (a–d). Both methods reveal CEZ with a Cr fraction as high as 20 at.%, which is in good agreement with the Cr gradients predicted by DICTRA in Fig. 10 (c). After further holding at 1000 °C, residual ferrite in the CEZ eventually transforms into austenite if the Cr content of the CEZ falls below the threshold value dictated by thermodynamic conditions presented in Fig. 11 (b). The presence of CEZ was recently investigated by Belde et al. [73] who observed Cr content above 20 wt.% after flash dissolution of  $M_{23}C_6$  in a Fe-11Cr-0.3C stainless steel.

**5. Conclusion**

Ferrite to austenite transformation and simultaneous  $M_{23}C_6$  (M=Fe, Cr) dissolution in MSS were studied using a combined experimental and modelling approach. A considerable fraction (5 vol.%

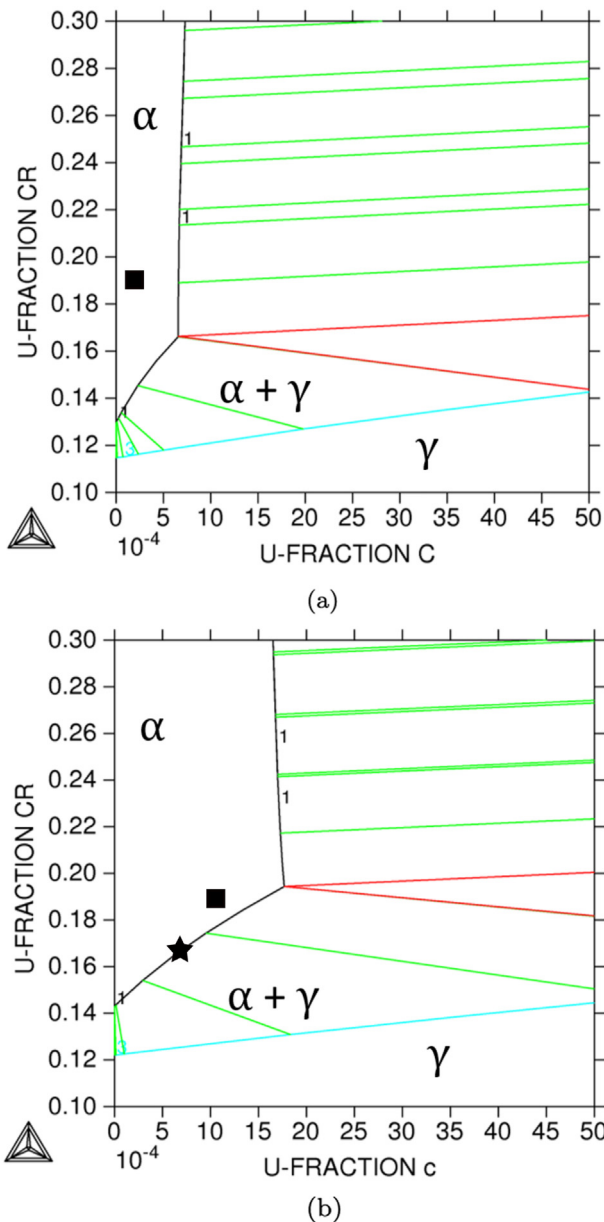


**Fig. 11.** Isothermal section of ternary Fe-Cr-C phase diagram at a) 900°C and b) 1000°C. The average composition of residual ferrite at 900°C (■) and after 10 s holding at 1000°C (★) suggests the stabilization of ferrite as the result of Cr enrichment.

to 20 vol.%) of ferrite remains untransformed after prolonged heat treatment in the austenitic temperature range. Based on the simulations results, the austenization kinetics can be rationalized in three stages, each one characterized by remarkably different austenite growth rate:

- Stage I: fast austenite growth, mainly controlled by rapid diffusion of Cr in the ferrite, which transforms up to 95 vol.% of ferrite into austenite.
- Stage II: simultaneous dissolution of  $M_{23}C_6$  particles and rapid increase of the Cr content in the ferrite which results in soft-impingement and transformation stasis.
- Stage III: homogenization and decrease of Cr content in the ferrite which allows for new austenite growth, now driven by slow diffusion of Cr in the bulk austenite.

Austenization is found to be sensitive to both process and microstructure parameters. Higher heating rates and larger initial particle sizes increase the extent of Cr enrichment in ferrite, leading to a stronger soft-impingement and formation of Chromium-Enriched-Zone (CEZ), which stabilizes residual ferrite to temperatures well within the austenite stability region for the nominal steel composition. On the other hand, slow heating rate and smaller initial particle size result in ferrite-free microstructures.

Recent findings on the same alloy showed how the mechanical strength contrasts between the softer ferrite phase and the surrounding martensite matrix is the leading cause of damage evolution in the softer phase [24], which decreases the overall ductility of the alloy. Hence, this work could open interesting pathways for the optimization of hot-stamping process conditions of MSS to design ductile microstructures with reduced amounts of residual ferrite.

#### Data availability

The raw data required to reproduce these findings are available to download from the 'dat' network (<https://datproject.org/>): [dat://7fef8fd34d33a7cc15dcf726609aa6b4e0290fda7c34841407f07ed2aaaeb166/]. The processed data required to reproduce these are available to download from the 'dat' network (<https://datproject.org/>): [dat://7fef8fd34d33a7cc15dcf726609aa6b4e0290fda7c34841407f07ed2aaaeb166/].

#### CRedit authorship contribution statement

**Alvise Miotti Bettanini:** Conceptualization, Methodology, Software, Validation, Investigation, Writing - original draft, Writing - review & editing, Visualization, Data curation. **Lipeng Ding:** Investigation. **Jean-Denis Mithieux:** Resources, Writing - review & editing, Supervision. **Coralie Parrens:** Writing - review & editing. **Hosni Idriissi:** Writing - review & editing. **Dominique Schryvers:** Writing - review & editing. **Laurent Delannay:** Writing - review & editing, Supervision, Project administration. **Thomas Pardoën:** Writing - review & editing, Supervision. **Pascal J. Jacques:** Conceptualization, Writing - review & editing, Supervision, Project administration.

#### Acknowledgement

The authors thank Professor Anne-Francoise Gourgues-Lorenzon and Helene Godin, Ecole Nationale Supérieure des Mines de Paris (MINES ParisTech) for their fruitful discussions. AMB thanks Stijn Van den broek (Universiteit Antwerpen) for the skillful preparation of TEM samples with FIB. The financial support of CBMM (Companhia Brasileira de Metalurgia e Mineracao) is gratefully acknowledged. L. Delannay is mandated by the FNRS-Belgium.

Computational resources have been provided by the supercomputing facilities of the UCLouvain (CISM/UCL) and the Consortium des Equipements de Calcul Intensif en Fédération Wallonie Bruxelles (CÉCI) funded by the Fond de la Recherche Scientifique de Belgique (F.R.S.-FNRS) under convention 2.5020.11.

#### References

- [1] D.S. Codd, *Automotive Mass Reduction with Martensitic Stainless Steel*, SAE International. 2011.
- [2] G. Badinier, C.W. Sinclair, X. Sauvage, X. Wang, V. Bylik, M. Gouné, F. Danoix, Microstructural heterogeneity and its relationship to the strength of martensite, *Mater. Sci. Eng. A* 638 (2015) 329–339.
- [3] F. Ruel, P.-O. Santacreu, S. Saedlou, G. Badinier, J. Herbelin, Corrosion Aspects Regarding the Use of Martensitic Stainless Steels in Automotive Chassis Parts, SAE International. 2015.
- [4] P.-O. Santacreu, G. Badinier, J.-B. Moreau, J.-M. Herbelin, Fatigue Properties of a New Martensitic Stainless Steel for Hot Stamped Chassis Parts, SAE International. 2015.

- [5] G. Krauss, Deformation and fracture in Martensitic carbon steels tempered at low temperatures, *Metall. Mater. Trans. A* 32B (2001) 1–17.
- [6] G. Krauss, Martensite in steel: strength and structure, *Mater. Sci. Eng. A* 273–275 (1999) 40–57.
- [7] A.J. Deardo, Niobium in modern steels, *Int. Mater. Rev.* 48 (6) (2003) 371–402.
- [8] R. Honeycombe, H.K.D.H. Bhadeshia, *Steel Microstructure and Properties*, Elsevier, 2006.
- [9] A. Pineau, A.A. Benzerga, T. Pardoen, Failure of metals I – brittle and ductile fracture, *Acta Mater.* 107 (2016) 424–483.
- [10] H. Ghadbeigi, C. Pinna, S. Celotto, Failure mechanisms in DP600 steel: initiation, evolution and fracture, *Mater. Sci. Eng. A* 588 (2013) 420.
- [11] H. Ghadbeigi, C. Pinna, S. Celotto, J.R. Yates, Local plastic strain evolution in a high strength dual-phase steel, *Mater. Sci. Eng. A* 527 (18–19) (2010) 5026.
- [12] Q. Han, A. Asgari, P.D. Hodgson, N. Stanford, Strain partitioning in dual-phase steels containing tempered martensite, *Mater. Sci. Eng. A* 611 (C) (2014) 90–99.
- [13] J. Kang, Y. Ososkov, J. Embury, D. Wilkinson, Digital image correlation studies for microscopic strain distribution and damage in dual phase steels, *Scr. Mater.* 56 (11) (2007) 999–1002.
- [14] G. Avramovic-Cingara, Y. Ososkov, M.K. Jain, D.S. Wilkinson, Effect of martensite distribution on damage behaviour in DP600 dual phase steels, *Mater. Sci. Eng. A* 516 (1–2) (2009) 7–16.
- [15] C. Landron, O. Bouaziz, E. Maire, J. Adrien, Characterization and modeling of void nucleation by interface decohesion in dual phase steels, *Scr. Mater.* 63 (10) (2010) 973–976.
- [16] Q. Lai, O. Bouaziz, M. Gouné, L. Brassart, M. Verdier, G. Parry, A. Perlede, Y. Bréchet, T. Pardoen, Damage and fracture of dual-phase steels: influence of martensite volume fraction, *Mater. Sci. Eng. A* 646 (C) (2015) 322–331.
- [17] S.K. Yerra, G. Martin, M. Véron, Y. Bréchet, J.D. Mithieux, L. Delannay, T. Pardoen, Ductile fracture initiated by interface nucleation in two-phase elastoplastic systems, *Eng. Fract. Mech.* 102 (2013) 77–100.
- [18] C.C. Tasan, M. Diehl, D. Yan, M. Bechtold, F. Roters, L. Schemmann, C. Zheng, N. Peranio, D. Ponge, M. Koyama, K. Tsuzaki, D. Raabe, An overview of dual-phase steels: advances in microstructure-oriented processing and micromechanically guided design, *Annu. Rev. Mater. Res.* 45 (1) (2015) 391–431.
- [19] C.C. Tasan, J.P.M. Hoefnagels, M. Diehl, D. Yan, F. Roters, D. Raabe, Strain localization and damage in dual phase steels investigated by coupled in-situ deformation experiments and crystal plasticity simulations, *Int. J. Plast.* 63 (C) (2014) 198–210.
- [20] G.R. Speich, V.A. Demarest, R.L. Miller, Formation of austenite during intercritical annealing of dual-phase steels, *Metall. Trans. A* 12 (8) (1981) 1419.
- [21] T.W.J. de Geus, F. Maresca, R.H.J. Peerlings, M.G.D. Geers, Microscopic plasticity and damage in two-phase steels: on the competing role of crystallography and phase contrast, *Mech. Mater.* 101 (C) (2016) 147–159.
- [22] M.C. Jo, J. Park, S.S. Sohn, S. Kim, J. Oh, S. Lee, Effects of untransformed ferrite on Charpy impact toughness in 1.8-GPa-grade hot-press-forming steel sheets, *Mater. Sci. Eng. A* 707 (2017) 65–72.
- [23] A.M. Bettanini, L. Delannay, P.J. Jacques, T. Pardoen, G. Badinier, J.-D. Mithieux, Influence of microscopic strain heterogeneity on the formability of Martensitic stainless steel, *AIP Conference Proceedings* 1896, 2017, pp. 020010.
- [24] A.M. Bettanini, F. Hannard, J.-D. Mithieux, G. Badinier, P.J. Jacques, T. Pardoen, L. Delannay, Residual ferrite in martensitic stainless steels: the effect of mechanical strength contrast on ductility, *Mater. Sci. Eng. A* 731 (2018) 495–505.
- [25] M. Hillert, K. Nilsson, L.E. Torndahl, Effect of alloying elements on the formation of austenite and dissolution of cementite, *J. Iron Steel Inst.* 209 (1971) 49–68.
- [26] L. Karmazin, Experimental study of the austenitization process of hypereutectoid steel alloyed with small amounts of silicon, manganese and chromium, and with an initial structure of globular cementite in a ferrite matrix, *Mater. Sci. Eng. A* 142 (1) (1991) 71–77.
- [27] L. Karmazin, J. Krejci, The dependence of the austenitization kinetics on the type of initial spheroidized structure in low alloy steel, *Mater. Sci. Eng. A* 185 (1994) L5–L7.
- [28] G. Miyamoto, J. Oh, K. Hono, T. Furuhashi, T. Maki, Effect of partitioning of Mn and Si on the growth kinetics of cementite in tempered Fe–0.6 mass% C martensite, *Acta Mater.* 55 (15) (2007) 5027.
- [29] G. Miyamoto, H. Usuki, Z.D. Li, T. Furuhashi, Effects of Mn, Si and Cr addition on reverse transformation at 1073 K from spheroidized cementite structure in Fe–0.6 mass% C alloy, *Acta Mater.* 58 (13) (2010) 4492–4502.
- [30] Z.-D. Li, G. Miyamoto, Z.-G. Yang, T. Furuhashi, Kinetics of reverse transformation from pearlite to austenite in an Fe–0.6mass% C alloy and the effects of alloying elements, *Metall. Mater. Trans. A* 42 (6) (2010) 1586–1596.
- [31] R. Wei, M. Enomoto, R. Hadian, H.S. Zurob, R. Hadian, G.R. Purdy, Growth of austenite from as-quenched martensite during intercritical annealing in an Fe–0.1C–3Mn–1.5Si alloy, *Acta Mater.* 61 (2) (2013) 697–707.
- [32] Y. Xia, M. Enomoto, Z. Yang, Z. Li, C. Zhang, Effects of alloying elements on the kinetics of austenitization from pearlite in Fe–C–M alloys, *Philos. Mag.* 93 (9) (2013) 1095–1109.
- [33] N. Nakada, K. Mizutani, T. Tsuchiyama, S. Takaki, Difference in transformation behavior between ferrite and austenite formations in medium manganese steel, *Acta Mater.* 65 (C) (2014) 251–258.
- [34] M. Enomoto, K. Hayashi, K. Hayashi, Simulation of the growth of austenite during continuous heating in low carbon iron alloys, *J. Mater. Sci.* 50 (20) (2015) 6786–6793.
- [35] Z.N. Yang, M. Enomoto, C. Zhang, Z.G. Yang, Transition between alloy–element partitioned and non-partitioned growth of austenite from a ferrite and cementite mixture in a high-carbon low-alloy steel, *Philos. Mag. Lett.* 96 (7) (2016) 256–264.
- [36] G.-H. Zhang, J.-Y. Chae, K.-H. Kim, D.-W. Suh, Effects of Mn, Si and Cr addition on the dissolution and coarsening of pearlitic cementite during intercritical austenitization in Fe–1 wt.%C alloy, *Mater. Charact.* 81 (2013) 56–67.
- [37] C.R. Hutchinson, H.S. Zurob, Y. Bréchet, The growth of ferrite in Fe–C–X alloys: the role of thermodynamics, diffusion, and interfacial conditions, *Metall. Mater. Trans. A* 37 (6) (2006) 1711.
- [38] H.I. Aaronson, W.T. Reynolds, G.R. Purdy, Coupled-solute drag effects on ferrite formation in Fe–C–X systems, *Metall. Mater. Trans. A* 35 (4) (2004) 1187.
- [39] C. Celada Casero, D. San Martín, Austenite formation in a cold-rolled semi-austenitic stainless steel, *Metall. Mater. Trans. A* 45 (4) (2013) 1767–1777.
- [40] S. Zhang, P. Wang, D. Li, Y. Li, Investigation of the evolution of retained austenite in Fe–13%Cr–4%Ni martensitic stainless steel during intercritical tempering, *Mater. Des.* 84 (2015) 385–394.
- [41] J.D. Escobar, J.D. Poplawsky, G.A. Faria, J. Rodriguez, J.P. Oliveira, C.A. Salvador, P.R. Mei, S.S. Babu, A.J. Ramirez, Compositional analysis on the reverted austenite and tempered martensite in a Ti-stabilized supermartensitic stainless steel: segregation, partitioning and carbide precipitation, *Mater. Des.* 140 (2018) 95–105. <https://doi.org/10.1016/j.matdes.2017.11.055>.
- [42] Q. Lai, M. Gouné, A. Perlede, T. Pardoen, P. Jacques, O. Bouaziz, Y. Bréchet, Mechanism of austenite formation from spheroidized microstructure in an intermediate Fe–0.1C–3.5Mn steel, *Metall. Mater. Trans. A* 47 (7) (2016) 3375–3386.
- [43] A. Bojack, L. Zhao, P.F. Morris, J. Sietsma, Austenite formation from martensite in a 13Cr6Ni2Mo supermartensitic stainless steel, *Metall. Mater. Trans. A* 47 (5) (2016) 1996.
- [44] R. Kapoor, I.S. Batra, On the  $\alpha'$  to  $\gamma$  transformation in maraging (grade 350), PH 13–8 Mo and 17–4 PH steels, *Mater. Sci. Eng. A* 371 (1–2) (2004) 324.
- [45] F. Niessen, M. Villa, J. Hald, M.A. Somers, Kinetics analysis of two-stage austenitization in supermartensitic stainless steel, *Mater. Des.* 116 (2017) 8.
- [46] A. Borgenstam, A. Engström, J. Ågren, L. Höglund, DICTRA, a tool for simulation of diffusional transformations in alloys, *J. Phase Equilib.* 21 (2003) 1–12.
- [47] A. Bhattacharya, C.S. Upadhyay, S. Sangal, A quantitative phase-field simulation of soft-impingement in austenite to ferrite transformation with mixed-mode, *Metall. Mater. Trans. A* 48 (10) (2017) 4929.
- [48] S.E. Offerman, N.H. van Dijk, J. Sietsma, S. Grigull, E.M. Lauridsen, L. Margulies, H.F. Poulsen, M.T. Rekveldt, S. van der Zwaag, Grain nucleation and growth during phase transformations, *Science* 298 (5595) (2002) 1003.
- [49] D.Z. Li, N.M. Xiao, Y.J. Lan, C.W. Zheng, Y.Y. Li, Growth modes of individual ferrite grains in the austenite to ferrite transformation of low carbon steels, *Acta Mater.* 55 (18) (2007) 6234.
- [50] C. Garcia, L.F. Alvarez, M. Carsi, Effects of heat-treatment parameters on non-equilibrium transformations and properties of X45Cr13 and X60Cr14MoV martensitic stainless steels, *Weld. Int.* 6 (8) (1992) 612–621.
- [51] D.V. Shtansky, K. Nakai, Y. Ohmori, Crystallography and structural evolution during reverse transformation in an Fe–17Cr–0.5C tempered martensite, *Acta Mater.* 48 (8) (2000) 1679.
- [52] D.V. Shtansky, K. Nakai, Y. Ohmori, Pearlite to austenite transformation in an Fe–2.6Cr–1C alloy, *Acta Mater.* 47 (9) (1999) 2619–2632.
- [53] D.V. Shtansky, K. Nakai, Y. Ohmori, Formation of austenite and dissolution of carbides in Fe–8.2Cr–C alloys, *Z. Met.* 90 (1) (1999) 25–37.
- [54] A. Bénéteau, A. Bénéteau, P. Weisbecker, G. Geandier, P. Weisbecker, E. Aebly-Gautier, G. Geandier, B. Appolaire, E. Aebly-Gautier, B. Appolaire, Austenitization and precipitate dissolution in high nitrogen steels: an in situ high temperature X-ray synchrotron diffraction analysis using the Rietveld method, *Mater. Sci. Eng. A* 393 (1–2) (2005) 63–70.
- [55] W. Song, P.-P. Choi, G. Inden, U. Prah, D. Raabe, W. Bleck, On the spheroidized carbide dissolution and elemental partitioning in high carbon bearing steel 100Cr6, *Metall. Mater. Trans. A* 45 (2) (2013) 595–606.
- [56] Q. Huang, O. Volkova, H. Biermann, J. Mola, Dilatometry analysis of dissolution of Cr-rich carbides in martensitic stainless steels, *Metall. Mater. Trans. A* 48 (12) (2017) 5771–5777.
- [57] R. Kapoor, L. Kumar, I.S. Batra, A dilatometric study of the continuous heating transformations in 18 wt.% Ni maraging steel of grade 350, *Mater. Sci. Eng. A* 352 (1–2) (2003) 318.
- [58] ASTM A1033-10(2015), Standard Practice for Quantitative Measurement and Reporting of Hypoeutectoid Carbon and Low-Alloy Steel Phase Transformations.
- [59] M.D. Abramoff, P.J. Magalhaes, S. Ram, Image processing with ImageJ, *Biophoton. Int.* 11 (7) (2004) 36–42.
- [60] M. Tamura, Y. Haruguchi, M. Yamashita, Y. Nagaoka, K. Ohinata, K. Ohnishi, E. Itoh, H. Ito, K. Shinozuka, H. Esaka, Tempering behavior of 9%Cr–1%Mo–0.2%V steel, *ISIJ Int.* 46 (11) (2006) 1693. <https://doi.org/10.2355/isijinternational.46.1693>.
- [61] J.O. Andersson, T. Helander, L. Höglund, P. Shi, Thermo-Calc & DICTRA, computational tools for materials science, *Calphad* 26 (2002) 273–312.
- [62] F. Christien, M.T. Telling, K.S. Knight, A comparison of dilatometry and in-situ neutron diffraction in tracking bulk phase transformations in a martensitic stainless steel, *Mater. Charact.* 82 (2013) 50–57.
- [63] A. Bojack, L. Zhao, P.F. Morris, J. Sietsma, In-situ determination of austenite and martensite formation in 13Cr6Ni2Mo supermartensitic stainless steel, *Mater. Charact.* 71 (2012) 77.
- [64] R. Rahimi, P. Pekker, H. Biermann, O. Volkova, B.C. De Cooman, J. Mola, Volumetric changes associated with B2-(Ni,Fe)Al dissolution in an Al-alloyed ferritic steel, *Mater. Des.* 111 (2016) 640.
- [65] Nat. Bur. Stand (US) Monogr. 25, vol. 21, 1985, 62.
- [66] S.S. Babu, E.D. Specht, S.A. David, E. Karapetrova, P. Zschack, M. Peet, H.K.D.H. Bhadeshia, In-situ observations of lattice parameter fluctuations in austenite and transformation to bainite, *Metall. Mater. Trans. A* 36 (12) (2005) 3281.

- [67] P.E.J. Rivera-Díaz-Del-Castillo, S. van der Zwaag, J. Sietsma, A model for ferrite/pearlite band formation and prevention in steels, *Metall. Mater. Trans. A* 35 (2) (2004) 425.
- [68] Z.-K. Liu, L. Höglund, B. Jönsson, J. Ågren, An experimental and theoretical study of cementite dissolution in an Fe-Cr-C alloy, *Metall. Trans. A* 22 (8) (1991) 1745.
- [69] C.G. de Andrés, J.A. Jiménez, L.F. Alvarez, Splitting phenomena occurring in the martensitic transformation of Cr13 and CrMoV14 stainless steels in the absence of carbide precipitation, *Metall. Mater. Trans. A* 27 (7) (1996) 1799–1805.
- [70] V.A. Esin, B. Denand, Q. Le Bihan, M. Dehmas, J. Teixeira, G. Geandier, S. Denis, T. Sourmail, E. Aeby-Gautier, In situ synchrotron X-ray diffraction and dilatometric study of austenite formation in a multi-component steel: influence of initial microstructure and heating rate, *Acta Mater.* 80 (2014) 118–131.
- [71] Y.K. Lee, H.C. Shin, D.S. Leem, J.Y. Choi, W. Jin, C.S. Choi, Reverse transformation mechanism of martensite to austenite and amount of retained austenite after reverse transformation in Fe-3Si-13Cr-7Ni (wt-%) martensitic stainless steel, *Mater. Sci. Technol.* 19 (3) (2003) 393.
- [72] F.M.C. Cerda, I. Sabirov, C. Goulas, J. Sietsma, A. Monsalve, R.H. Petrov, Austenite formation in 0.2% C and 0.45% C steels under conventional and ultrafast heating, *Mater. Des.* 116 (2017) 448. <https://doi.org/10.1016/j.matdes.2016.12.009>.
- [73] M. Belde, H. Springer, G. Inden, D. Raabe, Multiphase microstructures via confined precipitation and dissolution of vessel phases: example of austenite in martensitic steel, *Acta Mater.* 86 (2015) 1–14.